Journal of ELECTRONIC MATERIALS, Vol. 44, No. 1, 2015
DOI: 10.1007/s11664-014-3473-y

Preparation, Characterization, and Ionic Transport Properties of Nanoscale $Ln_2Zr_2O_7$ (Ln = Ce, Pr, Nd, Sm, Gd, Dy, Er, and Yb) Energy Materials

SAM SOLOMON,[1,2] ANEESH GEORGE,[1] JIJIMON KUMPAKKATTU THOMAS,[1] and ANNAMMA JOHN[1]

1.—Department of Physics, Mar Ivanios College, Thiruvananthapuram 695015, India. 2.—e-mail: samdmrl@yahoo.com

Nanoparticles of lanthanide (Ln)-based zirconates have been prepared through the autoignited combustion technique. The structure of the system was analyzed by powder x-ray diffraction and vibrational spectroscopic tools. The compounds with Ln = Ce, Pr, Nd, Sm, and Gd have pyrochlore cubic structure, whereas those with Ln = Dy, Er, and Yb possess anion-deficient disordered cubic fluorite structure. The optical properties of the powder were analyzed using ultraviolet–visible spectroscopy. Pellets of the compounds were sintered in the range from 1325°C to 1530°C for 2 h. The surface morphology of sintered $Nd_2Zr_2O_7$ was analyzed by scanning electron microscopy. Impedance spectroscopic studies of the samples were carried out at different temperatures. The conductivity increased to the order of 10^{-2} S/m at 750°C, and the highest conductivity of 13.21×10^{-2} S/m was obtained for $Er_2Zr_2O_7$. All samples of this system are suitable candidates for fabrication of electrolytes for use in solid oxide fuel cells, particularly at moderate temperatures.

Key words: Nanoparticles, pyrochlore, fluorite, ionic conductor, fuel cells

INTRODUCTION

Solid oxide fuel cell (SOFC) technology is an eco-friendly method to generate electricity directly by oxidizing a fuel with high efficiency.[1–3] The ionic conductivity of solid electrolytes and the chemical stability of the electrode–electrolyte interface at elevated temperatures are factors affecting the performance of SOFCs.[2] These factors can be controlled by introducing structural features such as defects, dopants, and mixing of different phase materials.[4] Binary systems of the type $A_2B_2O_7$ mainly exhibit two structure types: (i) the pyrochlore structure (space group $Fd\bar{3}m$; $Z = 8$), and (ii) the anion-deficient disordered fluorite structure (space group $Fm\bar{3}m$; $Z = 4$).[5] The pyrochlore structure can be considered as being derived from the fluorite structure by removing one-eighth of the anions in such a way that the newly formed holes constitute a diamond lattice.[6] The oxide ion vacancies of the pyrochlore structure are ordered. Due to the vacancies, some oxide ions leave their lattice sites and occupy interstitial positions, creating the intrinsic Frenkel disorder which increases the ionic conductivity compared with the disordered fluorite phase of the same composition.[7] In the pyrochlore structure, the larger cations, i.e., the lanthanides occupying the A site, are eight-coordinated whereas the smaller cations, i.e., Zr/Ti/Hf occupying the B site, are six-coordinated.[6,8]

Mandal et al.[9,10] reported that the pyrochlore structure has a network consisting of corner-linked BO_6 octahedra with A atoms at interstices. The stability of pyrochlores depends on a ratio of the ionic radius of the A and B cation in the range from 1.46 to 1.78. Materials in which $r_A/r_B < 1.46$ show an anion-deficient disordered fluorite structure ($[AB]_2O_7$). In this structure, the A- and B-type cations are randomly distributed over the A and B sites and the oxygen vacancies are disordered on the anion sublattice. The transformation from the

(Received August 8, 2014; accepted October 11, 2014; published online October 31, 2014)

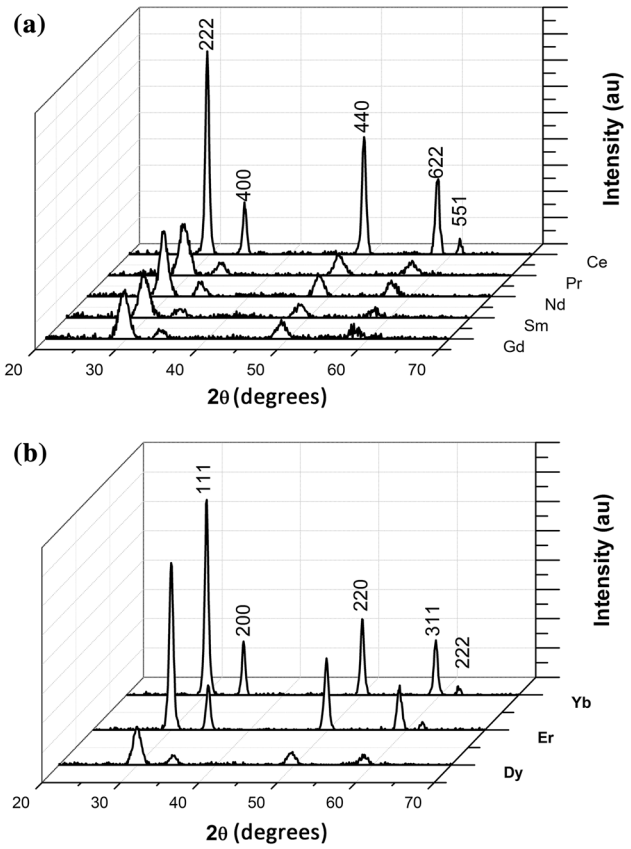

Fig. 1. XRD patterns of $Ln_2Zr_2O_7$: (a) Ln = Ce, Pr, Nd, Sm, and Gd, and (b) Ln = Dy, Er, and Yb.

Table I. Crystallographic data and particle size of $Ln_2Zr_2O_7$

RE	Ionic Radius (Å)	Lattice Constant, a (Å)	Cation Radius Ratio (r^{3+}/r^{4+})	Particle Size (nm)
Ce	1.143	10.65	1.586	16.91
Pr	1.126	10.60	1.564	8.45
Nd	1.109	10.57	1.540	9.63
Sm	1.079	10.51	1.496	10.22
Gd	1.053	10.45	1.463	9.87
Dy	1.027	5.18	1.426	8.87
Er	1.004	5.17	1.394	12.04
Yb	0.985	5.14	1.368	16.82

ordered pyrochlore to the anion-deficient disordered fluorite structure becomes energetically favorable as r_A/r_B decreases.[10] For materials with larger A cation and smaller B cation (region of compositional space with $r_A/r_B > 1.78$), the ordered pyrochlore structure is no longer the stable phase for $A_2B_2O_7$ materials, which will form the monoclinic structure.[11,12]

Kilner and Brook[13] reported that pyrochlores have superior conductivity, equivalent to that of

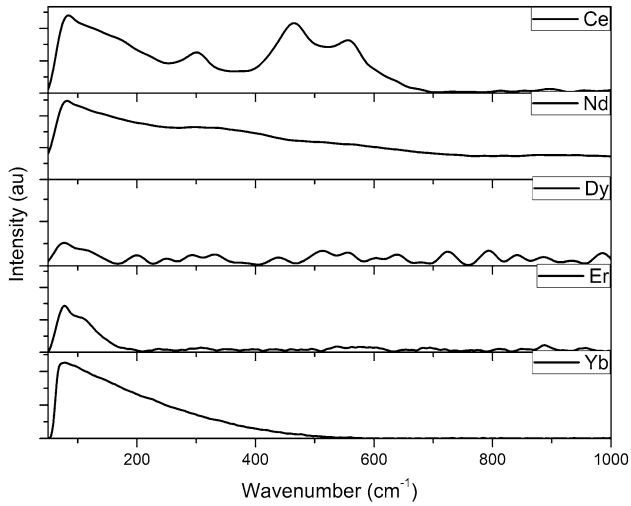

Fig. 2. FT Raman spectra of $Ln_2Zr_2O_7$ (Ln = Ce, Nd, Dy, Er, and Yb) over the range from 50 cm^{-1} to 1000 cm^{-1}.

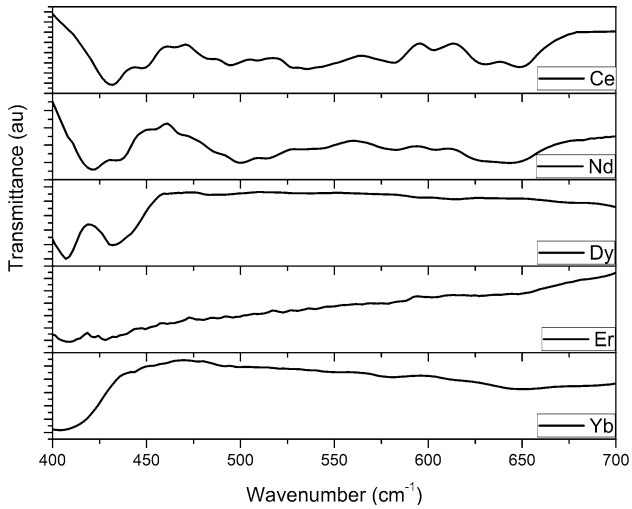

Fig. 3. FTIR spectra of $Ln_2Zr_2O_7$ (Ln = Ce, Nd, Dy, Er, and Yb) over the range from 400 cm^{-1} to 700 cm^{-1}.

some stabilized zirconia compositions at low temperatures. Shlyakhtina and Shcherbakova[14] reported that the oxygen ion conductivity of $A_2B_2O_7$ pyrochlores is influenced by the geometric factor r_A/r_B and the energetic factor of B–O bond covalency. According to Lian et al.,[15] the ionic conductivity of $Gd_2Zr_2O_7$ at 1000°C is 5 S/m. Yamamura et al.[16] explained that the compounds $RE_2Zr_2O_7$ with RE = Sm to Gd are the best oxide ion conductors with conductivity of around 8×10^{-1} S/m at 800°C. Shlyakhtina et al.[17] reported that the conductivity of $Sm_2Zr_2O_7$ at 780°C and 1 MHz is 5.0×10^{-1} S/m. Wilde and Catlow[18] indicated that the cation disorder in the pyrochlore structure is necessary for thermal generation of oxygen vacancies at the 48*f* site, according to their static energy minimization.

Table II. FT Raman spectral data (cm^{-1}) and band assignments for $Ln_2Zr_2O_7$ (Ln = Ce, Nd, Dy, Er, and Yb) over the range from 50 cm^{-1} to 1000 cm^{-1}

Wavenumber (cm^{-1})					
$Ce_2Zr_2O_7$	$Nd_2Zr_2O_7$	$Dy_2Zr_2O_7$	$Er_2Zr_2O_7$	$Yb_2Zr_2O_7$	Band Assignment
		985 w			$F_{2g}^{(1)}$
		885 w			
		842 w			
		791 s			
		726 m			
		639 w			
		604 w			
556 m	560 w	559 w	566 wbr		$F_{2g}^{(2)}$
	505 wbr	512 mbr			$F_{2g}^{(3)}$
463 s		437 w			A_{1g}
	340 mbr	333 wbr			$F_{2g}^{(4)}$
300 m	293 m	253 wbr	306 vwbr		E_g
		294 wbr			
84 s	82 s	195 w	112 s	76 s	Lattice modes
		117 m	73 vs		
		73 s			

Relative intensities: *v* very strong, *s* strong, *m* medium, *w* weak, *br* broad.

Table III. FTIR spectral data (cm^{-1}) and band assignments for $Ln_2Zr_2O_7$ (Ln = Ce, Nd, Dy, Er, and Yb) over the range from 400 cm^{-1} to 700 cm^{-1}

Wavenumber (cm^{-1})					
$Ce_2Zr_2O_7$	$Nd_2Zr_2O_7$	$Dy_2Zr_2O_7$	$Er_2Zr_2O_7$	$Yb_2Zr_2O_7$	Band Assignment
650 s	642 s		690 m	695 m	$F_{1u}^{(1)}$
630 s			650 m	648 m	
601 m	603 m			576 w	$F_{1u}^{(2)}$
580 s	581 m				
536 m	541 m				$F_{1u}^{(3)}$
527 m	513 s				
494 m	499 m				$F_{1u}^{(4)}$
449 s	438 s	432 m	427 s	406 s	$F_{1u}^{(5)}$
431 s	421 s	407 s	410 s		

Relative intensities: *s* strong, *m* medium, *w* weak.

In this paper, we report the preparation, characterization, and ionic transport properties of nanoscale lanthanide zirconates $Ln_2Zr_2O_7$ (Ln = Ce, Pr, Nd, Sm, Gd, Dy, Er, and Yb).

EXPERIMENTAL PROCEDURES

$Ln_2Zr_2O_7$ (Ln = Ce, Pr, Nd, Sm, Gd, Dy, Er, and Yb) nanoparticles were synthesized by the modified combustion method. In this method, a stoichiometric amount of Ce_2O_3, Pr_6O_{11}, Nd_2O_3, Sm_2O_3, Gd_2O_3, Dy_2O_3, Er_2O_3 or Yb_2O_3 is dissolved in concentrated nitric acid and $ZrOCl_2{\cdot}8H_2O$ in double-distilled water. To obtain the precursor complex, this stoichiometric solution is mixed with citric acid, keeping the citric acid to cation ratio at unity. The oxidant/fuel ratio of the system is adjusted by using concentrated HNO_3 and liquor ammonia, and the ratio is kept at unity. The product is stirred well for uniform mixing, and a clear solution with no precipitate or sedimentation is obtained. The solution containing the precursor mixture at pH ~7.0 is heated using a hot plate at ~250°C in a ventilated fume hood. The solution boils and undergoes dehydration followed by decomposition, leading to smooth deflation producing foam. On persistent heating, the foam autoignites due to self-propagating combustion, giving a voluminous fluffy powder. The obtained powder is annealed in oxygen atmosphere at 700°C to eliminate the trace amount of organic impurity that may remain in the sample.

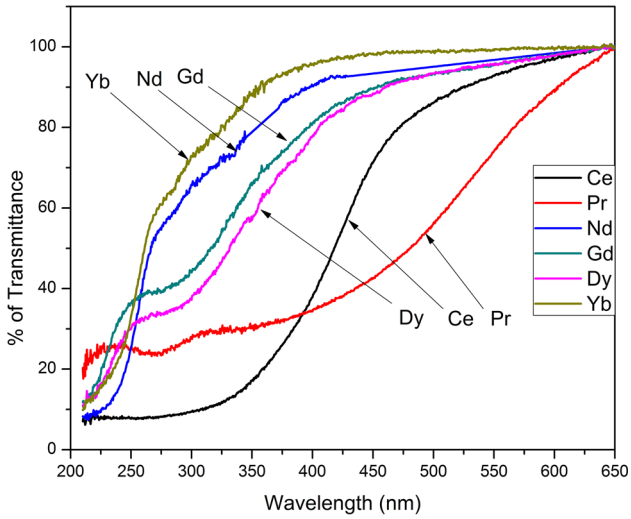

Fig. 4. UV–Vis transmittance spectra of $Ln_2Zr_2O_7$ (Ln = Ce, Pr, Nd, Gd, Dy, and Yb) over the range from 210 nm to 650 nm.

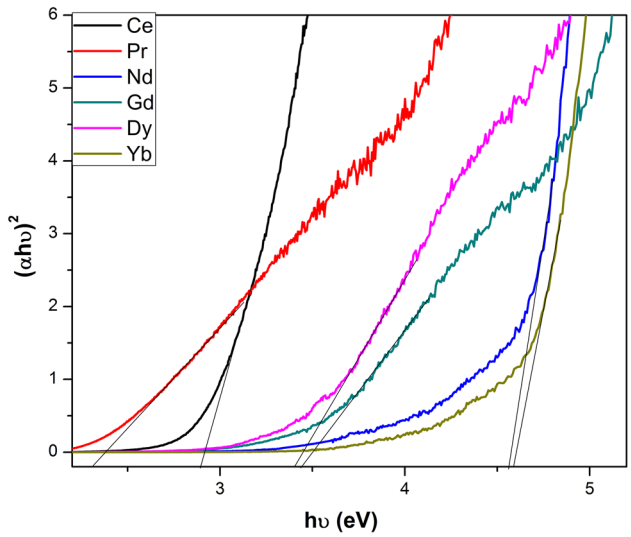

Fig. 5. Tauc plot of the optical absorption spectra at room temperature.

The structure of the as-prepared powders was identified by powder x-ray diffraction (XRD) analysis using a Bruker D8 x-ray diffractometer with nickel-filtered Cu K_α radiation. Fourier-transform (FT) Raman spectra of the samples were recorded at room temperature in the wavenumber range from 50 cm^{-1} to 1000 cm^{-1} using a Bruker RFS/100S spectrometer at power level of 150 mW and resolution of 4 cm^{-1}. Fourier-transform infrared (FTIR) spectra of the samples were recorded in the range from 400 cm^{-1} to 1000 cm^{-1} using a Thermo Nicolet Avatar 370 Fourier-transform infrared spectrometer by the KBr pellet method. Ultraviolet visible (UV–Vis) absorption spectra of the samples were recorded in the range from 200 nm to 650 nm using a Cary 100 BIO UV–Vis spectrophotometer.

Table IV. Sintering temperature and density of $Ln_2Zr_2O_7$ (Ln = Ce, Pr, Nd, Sm, Gd, Dy, Er, and Yb) nanoceramics

RE	Sintering Temperature (°C)	Density (g/cm^3)	% of Density
Ce	1325	5.93	94
Pr	1500	6.08	97
Nd	1440	6.17	97
Sm	1530	6.07	91
Gd	1480	6.03	91
Dy	1470	6.18	90
Er	1500	6.31	90
Yb	1510	6.89	92

The powder was then pressed into discs of thickness 2 mm and diameter 12 mm using a hydraulic press at pressure of 100 MPa, and sintered at higher temperature ranging from 1325°C to 1530°C for 2 h. The surface morphology and energy-dispersive x-ray spectra (EDS) of the sintered samples were studied using a JEOL 6390 LV scanning electron microscope (SEM). A sintered pellet was made into the form of a disc capacitor electrode by applying silver paste, and impedance spectroscopic study was carried out using an Hioki 3532 50 LCR meter in the frequency range from 50 Hz to 5 MHz.

RESULTS AND DISCUSSION

The XRD patterns of the $Ln_2Zr_2O_7$ (Ln = Ce, Pr, Nd, Sm, Gd, Dy, Er, and Yb) nanoceramics are shown in Fig. 1a and b. In Fig. 1a, all the reflections are indexed using International Centre for Diffraction Data (ICDD) files 52-1104, 20-1362, 78-1618, 24-1012, and 79-1146. The compounds with Ln = Ce, Pr, Nd, Sm, and Gd had pyrochlore cubic structure with space group $Fd\bar{3}m$. In Fig. 1b, all the peaks are indexed using ICDD files 72-1293, 78-1299, and 78-1300. The samples with Ln = Dy, Er, and Yb had cubic anion-deficient disordered fluorite structure with space group $Fm\bar{3}m$. The broadened peaks in the XRD patterns give a primary indication of the nanoscale nature of the materials.

The particle size and lattice parameters were calculated from the XRD patterns. The crystallographic data and ionic radius ratio (r^{3+}/r^{4+}, i.e., the ratio of the ionic radius of Ln to that of the Zr atom) are presented in Table I. Reflection from the (551) plane is observed only for the Ce compound, mainly due to the large cation radius ratio of this compound and its larger particle size. From this table, it is observed that the lattice constant a decreases as the ionic radius ratio increases. All the materials had particle size less than 17 nm. The lattice constant abruptly decreases to half when the composition changes from Gd to Dy, due to the structural change from the pyrochlore to fluorite structure.

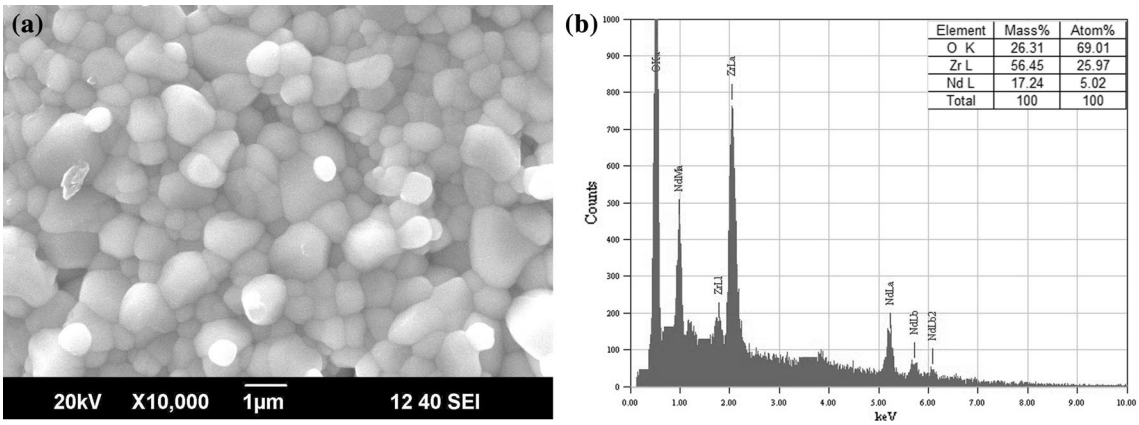

Fig. 6. (a) SEM image and (b) EDS pattern of $Nd_2Zr_2O_7$.

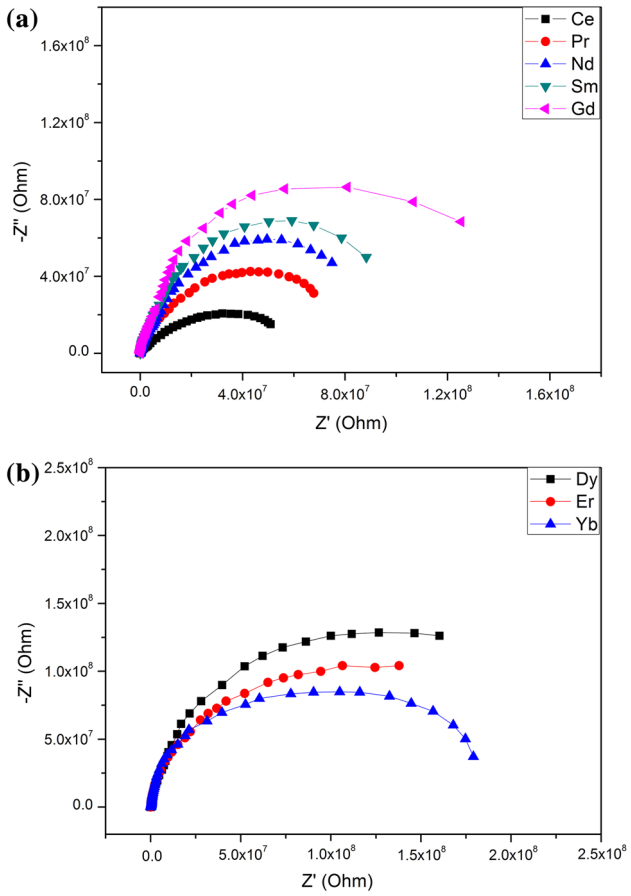

Fig. 7. Cole–Cole plots of $Ln_2Zr_2O_7$ at room temperature.

The pyrochlore structure $A_2B_2O_7$ with space group $Fd\bar{3}m$ and $Z = 8$ ($A_4B_4O_{12}O'_2$ for the primitive cell) can be described as a fluorite superstructure in which BO_6 octahedra are linked through corners to form a $[B_4O_{12}]_{infinite}$ framework in which an $[A_4O'_2]_{infinite}$ network of AO_4 tetrahedra with anti-p-cristobalite structure is imbricated. Factor group analysis of $A_2B_2O_7$ pyrochlores predicts six Raman-active modes ($A_{1g} + E_g + 4F_{2g}$) and seven IR-active modes ($7F_{1u}$). The cubic fluorite structure $A_2B_2O_7$ with space group $Fm\bar{3}m$ and $Z = 4$ has only one Raman-active mode (F_{2g}).[19]

The FT Raman and FTIR spectra of $Ln_2Zr_2O_7$ (Ln = Ce, Nd, Dy, Er, and Yb) are shown in Figs. 2 and 3, respectively. Tables II and III present the spectral data and band assignments of the Raman spectra and infrared spectra, respectively, of $Ln_2Zr_2O_7$ (Ln = Ce, Nd, Dy, Er, and Yb). The Raman spectrum for the Ce compound shows fairly intense and distinct bands at 300 cm^{-1}, 463 cm^{-1}, and 556 cm^{-1}. The strong band at 463 cm^{-1} is due to the O–Zr–O bending A_{1g} mode. The E_g mode due to ZrO_6 bending is obtained as a medium-intensity band at 300 cm^{-1}. The intense band at 556 cm^{-1} is due to the Zr–O stretching F_{2g} mode. The sharp intense band at 84 cm^{-1} accompanied by a continuum on the higher-wavenumber side extending up to around 250 cm^{-1} includes the lattice modes and the octahedral displacements. All the observed Raman bands show some amount of broadening. The band broadening is attributed to the disorder present in the ordered pyrochlore structure due to the presence of vacancies, defects, and foreign ions, which disrupts the translational symmetry of the lattice.[19] Figure 2 shows that the sharp features observed for $Ce_2Zr_2O_7$ are broadened when the rare earth is replaced by Nd, Dy or Er. Finally, the Raman spectrum for $Yb_2Zr_2O_7$ shows no single resolved band but only a scattering continuum starting from the band due to the lattice mode.[20,21]

The FTIR spectra of $Ln_2Zr_2O_7$ (Ln = Ce, Nd, Dy, Er, and Yb) show a behavior similar to that of the Raman spectra. The absorption bands are sharp and distinct in the case of $Ce_2Zr_2O_7$, and about five infrared (IR) characteristic bands are observed. In the spectra for the other compounds, the corresponding bands are diffuse and the broadening increases when Ce is replaced by Nd, Dy, Er or Yb.

Figure 4 shows the UV–Vis transmittance spectra of the $Ln_2Zr_2O_7$ (Ln = Ce, Pr, Nd, Gd, Dy, and Yb) nanoceramics. From these spectra, it is observed that the

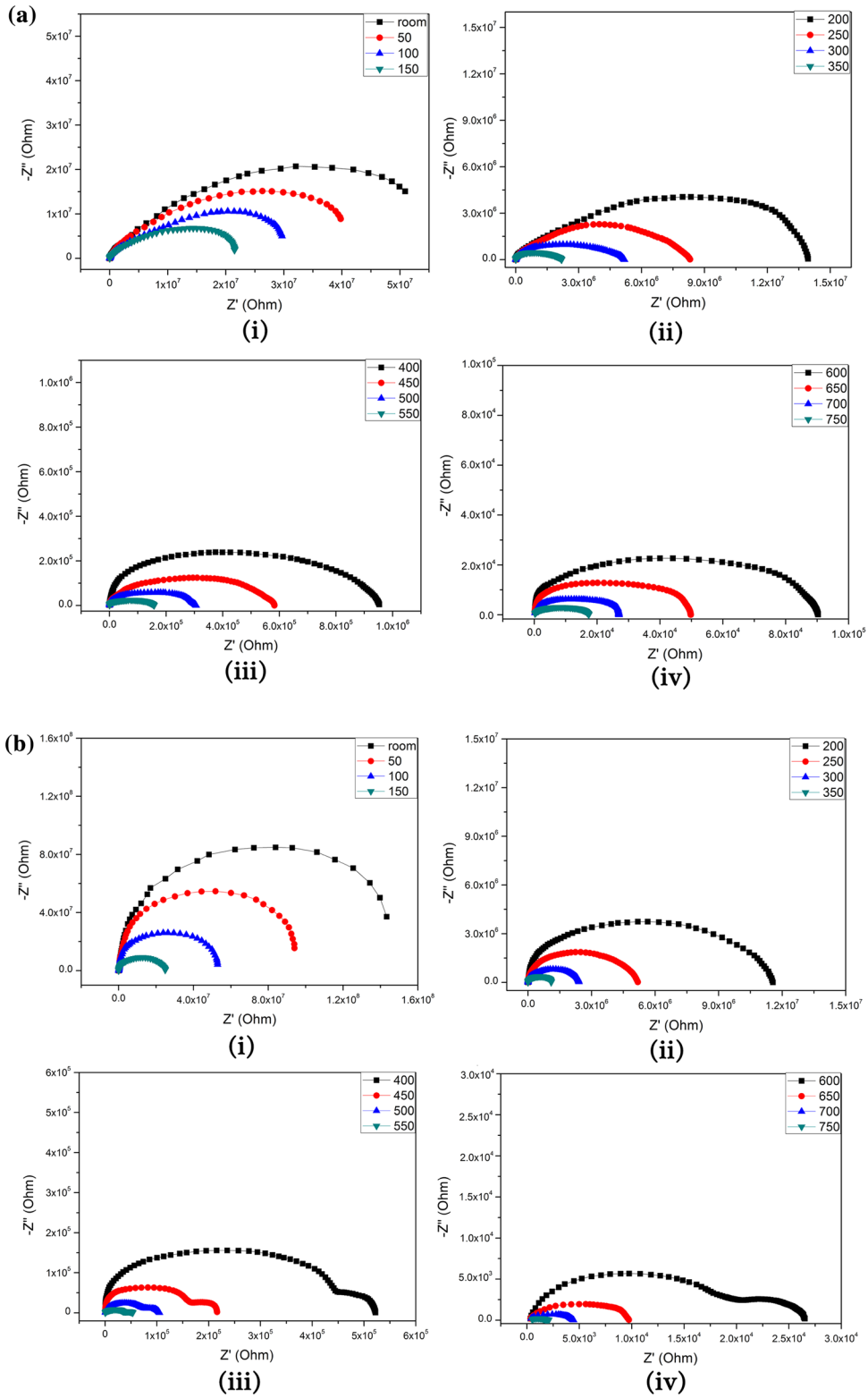

Fig. 8. Cole–Cole plots for (a) $Ce_2Zr_2O_7$ and (b) $Yb_2Zr_2O_7$ at different temperatures, and (c) semicircles fit to the experimental data at 600°C for the Ce and Yb compounds.

Nd and Gd compounds transmit heavily in the visible region. The Ce compound has very low transmittance in the ultraviolet (UV) region, moderate in the violet–blue region, and very high in the other regions of the visible range. The Pr compound shows moderate transmittance at UV wavelengths and the blue end of

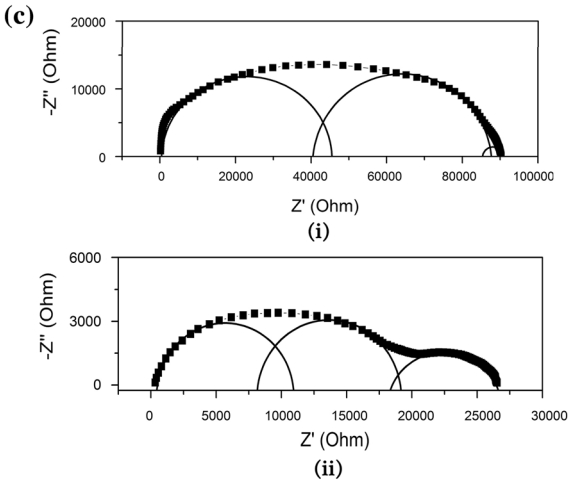

Fig. 8. continued.

the visible range, gradually increasing to a maximum at the red end. The spectrum for the Yb compound shows constant, high transmittance over the entire visible as well as UV regions, while for the Dy compound the transmittance decreases gradually with increase in frequency; this is due to absorption of photons in various energy levels of the 4*f* electrons of the lanthanide. The 4*f* orbitals are largely screened from external influences by electrons occupying orbitals with higher principal quantum number.[22] Therefore, the intensity of the 4*f* orbital absorption band is very low, resulting in the pale, pastel color of the samples. However, brown color is observed for the Pr compound, which is due to the high absorption in the visible range.

The absorption coefficient near the fundamental edge depends on the photon energy and obeys the Tauc equation. According to Tauc's relation, the absorption coefficient α for direct-bandgap materials is given by

$$\alpha(h\nu) = B(h\nu - E_g)^m, \quad (1)$$

where B is an energy-independent constant, α is the absorption coefficient, E_g is the optical bandgap energy, h is Planck's constant, ν is the frequency of the incident photon, and m is an index that depends on the nature of the electronic transition responsible for the optical absorption. The value of m for allowed direct transitions is 1/2.[23] Figure 5 shows a Tauc plot of the optical absorption spectra at room temperature. The optical bandgap energy obtained for the Ce, Pr, Nd, Gd, Dy, and Yb compounds was 2.92 eV, 2.30 eV, 4.56 eV, 3.42 eV, 3.35 eV, and 4.64 eV, respectively. The valance band and conduction band of $Ln_2Zr_2O_7$ consist of Ln 4*f* orbitals and Zr 4*d* orbitals. The energy gap between these two orbitals strongly depends on the crystallite size. The O 2*p* orbitals lie below the Ln 4*f* orbital and do not affect the bandgap of the materials. Hence, the quantum size effect and Ln 4*f* orbitals affect the bandgap, resulting in the variation of the bandgap energies for these nanoceramics.

The sintering behavior of the nanopowders synthesized by the presented combustion route was also studied. Compacted pellets were sintered for 2 h at various temperatures; the obtained densities and percentage density achieved are presented in Table IV. From this table, it is observed that all the samples sintered at very high temperature and achieved density above 90%. During nanoparticle sintering, grain boundary merging and grain growth take place. Due to the grain boundary merging, the sample density is lower than the theoretical value. Therefore, all the samples can be used for high-temperature electrical applications.

Figure 6a shows an SEM image of the $Nd_2Zr_2O_7$ compound. The image shows that the sample is well sintered with minimum porosity. The grains are well packed at the grain boundaries, and the average grain size determined from the micrograph is ~750 nm. The sintering temperature and time are the main factors that influence sintering. On sintering, the radius of curvature of the grain boundaries is directly proportional to the rate of grain growth and the inverse of grain size.[24–26] As a result of the higher surface-to-volume ratio of nanograin-size materials, the effective diffusivity is much higher. Therefore, nanocrystalline materials exhibit a strong driving force for grain growth and the temperature for sintering is reduced by 200°C to 300°C compared with the bulk.[27] Figure 6b shows EDS results for the sintered pellet; the spectrum clearly substantiates the presence of stoichiometric concentrations of the constituents of the specimen.

Figure 7 shows Cole–Cole impedance plots for the $Ln_2Zr_2O_7$ (Ln = Ce, Pr, Nd, Sm, Gd, Dy, Er, and Yb) compounds at room temperature. All the samples show extended semicircle behavior due to the combined contributions of grain, grain boundary, and specimen–electrode interface. When the cation radius ratio (r^{3+}/r^{4+}) decreases from 1.588 to 1.463, the structural symmetry of the crystal shows some distortion. This effect generates a barrier to hopping of ions through the sample at normal conditions. Therefore, the impedance increases. However, when r^{3+}/r^{4+} decreases from 1.426 to 1.368, the ordering of the cubic structure increases and hence the impedance decreases. The lower-particle-size material has higher surface states, generating a barrier to hopping of ions in the sample at normal condition. However, at higher temperatures, these effects enhance the transfer of thermally activated ions and increase the grain boundary conduction.

Figure 8 shows Cole–Cole plots for the Ce and Yb compounds at various temperatures in the range from room temperature to 750°C with step size of 50°C. As the temperature increases, the hopping mechanism of thermally activated ions also increases. Therefore, the impedance decreases. The observed graph is resolved into overlapping semicircles corresponding to the contributions of grain, grain boundary, and specimen–electrode interface. Generally a Cole–Cole plot contains three semicir-

Table V. Grain ("g") and grain boundary ("gb") parameters of $Ln_2Zr_2O_7$ at 750°C

RE	R_g (Ω)	C_g (F)	R_{gb} (Ω)	C_{gb} (F)	τ_g (s)	τ_{gb} (s)
Ce	825	1.03×10^{-10}	458	3.77×10^{-10}	8.49×10^{-8}	1.72×10^{-7}
Pr	1857	2.73×10^{-11}	1950	6.59×10^{-11}	5.07×10^{-8}	1.28×10^{-7}
Nd	157	8.89×10^{-10}	650	2.35×10^{-10}	1.39×10^{-7}	1.53×10^{-7}
Sm	357	1.46×10^{-10}	350	3.61×10^{-10}	5.23×10^{-8}	1.26×10^{-7}
Gd	957	4.70×10^{-11}	750	1.04×10^{-10}	4.49×10^{-8}	7.80×10^{-8}
Dy	750	8.35×10^{-11}	350	3.82×10^{-10}	6.26×10^{-8}	1.33×10^{-7}
Er	557	2.74×10^{-10}	350	4.84×10^{-10}	1.53×10^{-7}	1.69×10^{-7}
Yb	461	1.41×10^{-9}	646	2.62×10^{-10}	8.65×10^{-8}	1.69×10^{-7}

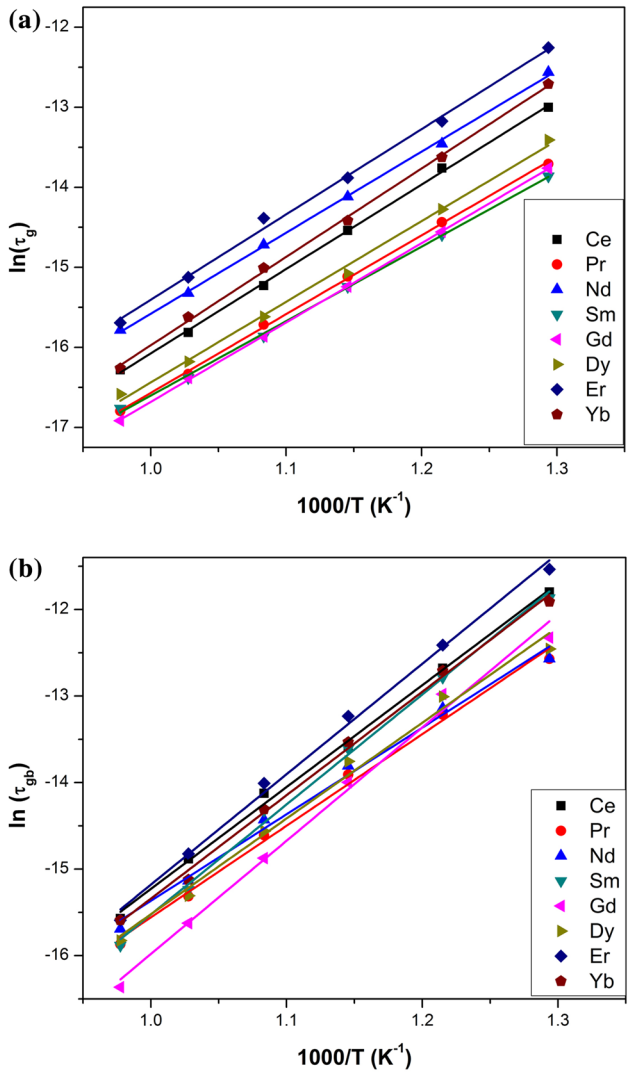

Fig. 9. Arrhenius plot of τ_g and τ_{gb} of $Ln_2Zr_2O_7$.

Table VI. Activation energy of grain and grain boundary

RE	E_{ag} (eV)	E_{agb} (eV)
Ce	0.91	1.02
Pr	0.85	0.91
Nd	0.87	0.86
Sm	0.80	1.09
Gd	0.86	1.13
Dy	0.87	0.95
Er	0.92	1.10
Yb	0.95	1.03

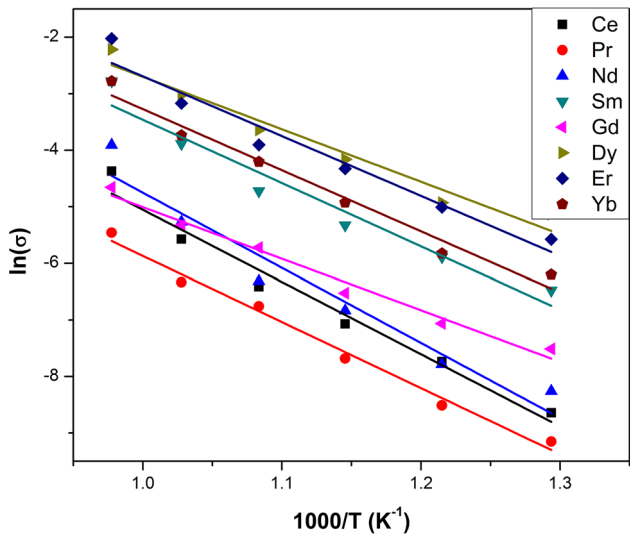

Fig. 10. Arrhenius plot of conductivity.

cles: the first (higher frequency) is due to the grain contribution, the second (intermediate frequency) is due to the grain-boundary contribution, and the last (lower frequency) is due to the electrode effect. For the Yb compound, above 400°C, the plots show depressed semicircles, indicating splitting into two semicircles. However, for the Ce compound, a very weak trace of the second semicircle is observed. The first extended semicircle is due to the combined contributions of grain and grain boundary conduction, whereas the second one is due to the electrode–specimen effect. The first semicircle was deconvoluted into two to separate the grain and grain-boundary contributions. Each semicircle can be resolved into a parallel combination of resistance (R) and capacitance (C) for the sample. The semicircles fit to the experimental data at 600°C for the Ce and Yb compounds are shown in Fig. 8c. The relaxation times for the grain and grain boundary polarizations

Table VII. Conductivity and activation energy of $Ln_2Zr_2O_7$ at 750°C

RE	$\sigma \times 10^{-2}$ (S/m)	E_a (eV)
Ce	1.26	1.10
Pr	0.45	1.01
Nd	2.01	1.14
Sm	6.23	0.96
Gd	0.95	0.84
Dy	10.89	0.91
Er	13.21	0.95
Yb	7.60	0.98

were calculated from the maximum of each semicircle in the Cole–Cole plot. Using the equation

$$\omega_{max}\tau = 1, \quad (2)$$

where $\tau = RC$ is the relaxation time,[28] the capacitance values were estimated for the maximum frequency of each semicircle. At lower temperatures, the relaxation process in the material mainly depends on immobile species/electrons, whereas at higher temperatures, it depends on defects/vacancies present in the sample. The relaxation time τ for grain and grain boundary were calculated from the semicircles corresponding to the grain and grain boundary contributions in the Cole–Cole plot. The calculated values of grain and grain boundary resistance, capacitance, and relaxation time at 750°C are presented in Table V.

The dielectric relaxation decreases with increase in temperature, showing Arrhenius behavior. Figure 9 shows an Arrhenius plot of τ_g and τ_{gb}. The activation energies calculated from the slopes of the Arrhenius plots are presented in Table VI. From this table, it is observed that the activation energy for grain boundary is greater than the activation energy for grain. This is because of the self-purification of nanoparticles. Therefore, all the defects are concentrated on the surface of the nanoparticles, which will reduce the relaxation time of hopping ions. At higher temperatures, the activation energy is greater than the energy required for vacancy creation and motion of charge carriers into vacancies.

The total ionic conductivity σ was calculated from the grain and grain boundary resistance using the relation

$$\sigma = t/AR, \quad (3)$$

where t is the thickness and A is the cross-sectional area of the material. As the temperature increases, the conductivity obeys the Arrhenius relation

$$\sigma = \sigma_0 \exp(-E_a/kT), \quad (4)$$

where σ_0 is the pre-exponential factor, E_a is the activation energy, and k is the Boltzmann constant.[29] Figure 10 shows the Arrhenius plot of conductivity. The conductivities obtained for all the compounds at 750°C are presented in Table VII. The conductivities obtained for all the compounds are in the range required for solid electrolytes.

CONCLUSIONS

Nanoparticles of the $Ln_2Zr_2O_7$ system (Ln = Ce, Pr, Nd, Sm, Gd, Dy, Er, and Yb) were prepared through the autoignited combustion technique. Structural analyses carried out using x-ray diffraction and vibrational spectroscopic methods were in good agreement with each other. All compounds had particle size less than 17 nm. The optical bandgap of the samples lay between 2.30 eV and 4.64 eV. Pelletized samples of the compounds were sintered to density above 90% of the theoretical density, possessing well-packed grains as evidenced by SEM. When the cation radius ratio (r^{3+}/r^{4+}) decreased from 1.588 to 1.463, the impedance increased due to distortion of the structural symmetry of the crystal, and when r^{3+}/r^{4+} decreased from 1.426 to 1.368, the ordering of the cubic structure increased and the impedance decreased. The conductivity of the samples was comparable to that required to fabricate SOFC electrolytes.

ACKNOWLEDGEMENTS

The authors acknowledge the Kerala State Council for Science, Technology, and Environment, Government of Kerala for financial assistance.

REFERENCES

1. Z.G. Liu, J.H. Ouyang, K.N. Sun, and Y. Zhou, *Ceram. Int.* 38, 2935 (2012).
2. L.C. Wen, H.Y. Hsieh, Y.H. Lee, S.C. Chang, H.C.I. Kao, H.S. Sheu, I.N. Lin, J.C. Chang, M.C. Lee, and Y.S. Lee, *Solid State Ion.* 206, 39 (2012).
3. Z.G. Liu, J.H. Ouyang, Y. Zhou, J. Xiang, and X.M. Liu, *Mater. Des.* 32, 4201 (2011).
4. J. Wang, F. Zhang, J. Lian, R.C. Ewing, and U. Becker, *Acta Mater.* 59, 1607 (2011).
5. E.J. Harvey, K.R. Whittle, G.R. Lumpkin, R.I. Smith, and S.A.T. Redfern, *J. Solid State Chem.* 178, 800 (2005).
6. W.E. Klee and G. Weitz, *J. Inorg. Nucl. Chem.* 31, 2367 (1969).
7. K.V. Govindan Kutty, C.K. Mathews, T.N. Rao, and U.V. Varadaraju, *Solid State Ion.* 80, 99 (1995).
8. S. Moll, G. Sattonnay, L. Thomé, J. Jagielski, C. Legros, and I. Monnet, *Nucl. Instrum. Methods B* 268, 2933 (2010).
9. B.P. Mandal, M. Pandey, and A.K. Tyagi, *J. Nucl. Mater.* 406, 238 (2010).
10. B.P. Mandal, N. Garg, S.M. Sharma, and A.K. Tyagi, *J. Nucl. Mater.* 392, 95 (2009).
11. G. Sattonnay, S. Moll, L. Thome, C. Legros, M. Herbst-Ghysel, F. Garrido, J.M. Costantini, and C. Trautmann, *Nucl. Instrum. Methods B.* 266, 3043 (2008).
12. M. Lang, F. Zhang, J. Zhang, J. Wang, J. Lian, W.J. Weber, B. Schuster, C. Trautmann, R. Neumann, and R.C. Ewing, *Nucl. Instrum. Methods B.* 268, 2951 (2010).
13. J.A. Kilner and R.J. Brook, *Solid State Ion.* 6, 237 (1982).
14. A.V. Shlyakhtina and L.G. Shcherbakova, *Solid State Ion.* 192, 200 (2011).
15. J. Lian, L. Wang, J. Chen, K. Sun, R.C. Ewing, J.M. Farmer, and L.A. Boatner, *Acta Mater.* 51, 1493 (2003).
16. H. Yamamura, H. Nishino, K. Kakinuma, and K. Nomura, *Solid State Ion.* 158, 359 (2003).

17. A.V. Shlyakhtina, A.V. Knotko, M.V. Boguslavskii, S.Yu. Stefanovich, I.V. Kolbanev, L.L. Larina, and L.G. Shcherbakova, *Solid State Ion.* 178, 59 (2007).
18. P.J. Wilde and C.R.A. Catlow, *Solid State Ion.* 112, 173 (1998).
19. B.P. Mandal, P.S.R. Krishna, and A.K. Tyagi, *J. Solid State Chem.* 183, 41 (2010).
20. H. Morisaka, T. Tant, H. Kaga, and K. Takatori, *J. Ceram. Soc. Jpn.* 112, 514 (2004).
21. F.N. Sayed, V. Grover, K. Bhattacharyya, D. Jain, A. Arya, C.G.S. Pillai, and A.K. Tyagi, *Inorg. Chem.* 50, 2354 (2011).
22. D.B. Dhwajam, J.K. Thomas, K. Joy, and S. Solomon, *J. Mater. Sci.* 22, 384 (2011).
23. A.S. Deepa, S. Vidya, P.C. Manu, S. Solomon, A. John, and J.K. Thomas, *J. Alloys Compd.* 509, 1830 (2011).
24. H. Gleiter, *Acta Mater.* 48, 1 (2000).
25. C.P. Cameron and R. Raj, *J. Am. Ceram. Soc.* 71, 1031 (1988).
26. V.V. Skorokhod and A.V. Ragulya, *Features of Nanocrystalline Structure Formation on Sintering of Ultra-Fine Powders* (The Netherlands: Kluwer Academic, 1998).
27. C. Suryanarayana, *JOM* 54, 24 (2002).
28. J.E. Kim, S.J. Kim, and Y.S. Yang, *Mater. Sci. Eng. A-Struct.* 304–306, 487 (2001).
29. A.R. Polu and R. Kumar, *Bull. Mater. Sci.* 34, 1063 (2011).